Applied Catalysis B: Environmental 231 (2018) 62–72

Contents lists available at ScienceDirect

Applied Catalysis B: Environmental

journal homepage: www.elsevier.com/locate/apcatb

An extensive study about influence of the carbon support morphology on Pt activity and stability for oxygen reduction reaction

Mariappan Sakthivel, Jean-Francois Drillet*

DECHEMA-Forschungsinstitut, 60486 Frankfurt am Main, Germany

ARTICLE INFO

Keywords:
Ordered mesoporous carbon
Pt/C catalyst
ORR
Accelerated degradation tests
DMFC

ABSTRACT

Several commercial carbons were tested with respect to their thermal stability and electrochemical activity as Pt catalyst support for oxygen reduction reaction (ORR). TGA analysis revealed that carbons with low BET surface such as graphite nanoparticles (GNP_{500}, 100 $m^2 g^{-1}$) are less prone to degradation than ordered mesoporous carbon (OMC, 1000 $m^2 g^{-1}$). Moreover, high Pt loading favored considerably carbon oxidation rate in air. Best results in terms of activity for ORR and stability during electrochemical accelerated degradation tests (ADT) were yielded by Pt/GNP_{500} and Pt/OMC, respectively. High graphitization level and mesoporous surface structure of carbon were found to be determinant for sustainable Pt stability. Addition of certain amount of PTFE to Nafion as binder in gas diffusion electrode (GDE) catalyst layer clearly improved electrochemical surface area (ECSA) retention. Comparative identical location TEM images of electrochemically-aged Pt on Vulcan and OMC demonstrated positive influence of mesoporous carbon surface on immobilization of catalyst particles and consequently on ECSA retention. After 10,000 ADT cycles, ECSA retention was close to 30% for Pt/OMC compared to about 1% for Pt/Vulcan. This was due to dramatic increase of Pt particle size on Vulcan support up to 40 nm compared to about 15 nm for Pt on OMC.

1. Introduction

Direct methanol fuel cell (DMFC) is a promising technology for energy supply of portable and stationary applications due to high energy density of methanol, compact design, easy fuel handling and storage. However, poor activity of Pt for methanol oxidation, low corrosion resistance of Pt/C at high cathodic voltage and methanol crossover that results on fuel loss mixed potential formation at the cathode are technical challenges to overcome [1]. Methanol efficiency up to about 80% can be yielded by using appropriate fuel concentration and applying high current density [2]. Long-term efficiency of the electrodes is strongly influenced by structural morphology and composition of the catalyst support that should allow optimal distribution and stabilization of the catalyst nanoparticles, anchorage of functional groups, good electronic conductivity, facile mass transport of reactants and products as well as high corrosion stability under oxidizing conditions [3,4]. Commonly, most of low and middle temperature fuel cells rely on low-cost mass-produced carbon black materials with predominant microporous domains (< 2 nm) that are mostly not or partially accessible for reactants, exposed to corrosion process and consequently severely affect catalyst performance and durability.

One of the main obstacles for widespread commercialization of proton exchange membrane fuel cells (PEMFC) is related to its insufficient long-term stability especially at high current densities [5]. Meanwhile five main mechanisms have been identified as causes for electrochemically active surface area (ECSA) degradation of Pt: (i) Ostwald ripening-based coarsening (dissolution of small metal particles and precipitation onto larger ones); (ii) migration on carbon support and coalescence; (iii) detachment, (iv) dissolution and precipitation in ionomer phase and (v) carbon corrosion. Pt dissolution mechanism is strongly influence by particle size and is governed by so-called Gibbs-Thomson effect [6,7]. Smaller particles have a higher surface energy, which causes a shift in the equilibrium dissolution potential to less positive values. Thus an exponential increase in dissolution rate with decreasing particle size was suggested, so that particles of diameters smaller than 2 nm are expected to dissolve at orders of magnitude faster than particles with diameters of for instance 5 nm. This is in accordance with some results issued from former identical location transmission electron microscope (IL-TEM) studies [8]. Huge impact of carbon nature and morphology on catalyst longevity is therefore well-admitted but still not fully understood. We recently demonstrated that adequate nature of carbon with middle BET surface (50–100 $m^2 g^{-1}$) combined with graphitic domains can drastically improve catalyst longevity for oxygen reduction reaction/ oxygen evolution reaction (ORR/OER) in

* Corresponding author.
E-mail address: drillet@dechema.de (J.-F. Drillet).

https://doi.org/10.1016/j.apcatb.2018.02.050
Received 7 December 2017; Received in revised form 9 February 2018; Accepted 21 February 2018
Available online 22 March 2018
0926-3373/

alkaline environment [9].

Because of its different micro textures and morphologies, carbon is still an attractive material for a large range of electrochemical applications [10]. Carbon as support material for nano disperse electrocatalyst should fulfill following criteria; (i) good electrical conductivity, (ii) suitable host for the catalyst particles and (iii) high corrosion stability under oxidizing conditions [3,4]. Proper choice of support material is determinant for performing and durable catalyst [11,12]. Ideally, carbon material should additionally possess predominantly mesoporous structure with large surface area, pore volume as well as narrow pore size distribution. The large surface area and 3D connected mono-dispersed mesospheres facilitates diffusion of the reactants, making them very attractive materials as fuel cell catalyst supports [13].

One discerns two types of mesoporous carbon: ordered (OMC) and disordered (DOMC) ones. OMCs are the most promising systems and therefore have been extensively studied as alternative catalyst support materials to micropore ones such as carbons black for fuel cells applications [14–16]. In particularly, graphitized carbon hollow spheres deserve unique features of good gas penetrability and optimal pore size distribution for nanoparticle confinement with improved activity for ORR and stability. The latter property was attributed to the presence of numerous graphitic domains [17]. Hayashi et al. [18] built an ideal triple-phase boundary inside the mesopores of carbon support in order to examine the electrochemical reactions at nanoscale. The effect of mesoporous carbons pore morphology on electrocatalytic activity of 20 wt% Pt was also studied [19] on OMC (CMK-3) and disordered wormhole mesoporous carbon (WMC). It was found that CMK-3 support provided more electrochemically active Pt sites and higher active surface area than WMC, leading to superior ORR activity and fuel cell performance. This enhanced catalytic activity was attributed to the highly ordered structure and good 3D interconnection of the nanospacings of carbon nanorods, resulting to higher catalyst utilization compared to WMCs. Lust et al. [20,21] studied activity of ordered micro-mesoporous tungsten and molybdenum carbide derived carbon (CDC) supported catalysts for ORR. Best results in terms of activity normalized to Pt mass amounted 27 A g^{-1} and was obtained with Pt–C(Mo_2C)800. Novel ordered hierarchical mesoporous/microporous carbon (OHMMC) derived from mesoporous titanium-carbide/carbon composites was prepared by synthesizing ordered mesoporous nanocrystalline titanium-carbide/carbon composites, followed by chlorination of titanium carbides and tested for supercapacitor applications [22].

Kim et al. [23] studied the durability of ordered mesoporous carbons OMC-supported (CMK-3, CMK-3G, and CMK-5) Pt catalysts in the potential range from 0.6 to 1.2 V at 50 mV s^{-1} for 2000 cycles. Highly graphitized CMK-3G was less prone to formation of surface oxygen functional groups during potential cycling compared to CMK-3 and CMK-5 (amorphous-carbon-like frameworks). They claimed that mass activity of the catalysts is nearly inversely proportional to micropore volume of the carbon supports. Grozovski et al. [24] measured about 80 mV less overpotential for ORR on microporous–mesoporous carbons-supported Pt (100) nanocubes compared to Pt(100) on Vulcan. Maiyalagan et al. [25] observed a threefold higher mass activity of 3D cubic OMC-supported (CMK-8) Pd (486 mA mg^{-1}) at 0.3 V for ORR in 0.5 M HCOOH + 0.5 M H_2SO_4 compared to that of Pt/C. By using a hard-template route, Galeano et al. [17,26] have developed mesoporous highly graphitized carbon hollow spheres with a specific surface area of about 1000 m^2 g^{-1} and average pore size distribution in the range of 3–4 nm that allow perfect Pt nanoparticles confinement and slow down degradation processes such as particle detachment and coalescence. Another interesting strategy aims at the development of catalyst-free catalysts. Popov and coworkers [27] synthesized N-doped ordered mesoporous carbon (CNx) via a nanocasting process by using polyacrylonitrile (PAN) as nitrogen and carbon precursors while mesoporous silica served as template. After a pyrolysis process in argon at 1000 °C, a current density of 0.6 A cm^{-2} at 0.5 V was obtained in a H_2/O_2 PEFC using 2 mg cm^{-2} catalyst loading.

Table 1
BET and average pore diameter values of the different carbons used in this work (data provided by manufacturer).

Product name	Description	Supplier	BET surface $m^2 g^{-1}$	Avg. pore size nm	Avg. particle size nm
Vulcan	Carbon black	Cabot	240	2	50
$HSAG_{300}$	High Surface Area Graphite	TIMCAL	250	–	15
OMC	Ordered Mesoporous Carbon	ACS Material®	1000	3.9-5.5	500-5000
GNP_{10}	Graphite Nano Particles	ACS Material®	660-720	–	10
GNP_{500}	Graphitized Nano Particles	Sigma Aldrich	100	6.4	50

This work aims at the study of highly active and corrosion-resistant Pt/C catalyst for the middle-temperature (120–150 °C) DMFC cathode. First results about preliminary screening of several as-prepared and commercial available carbon/graphite-supported 40 wt% Pt catalysts regarding their activity for ORR under rotating ring disk electrode (RRDE) and gas diffusion electrode (GDE) cell conditions as well as their stability under accelerated stress tests are presented.

2. Experimental

The commercial available carbon materials tested in this work were used as received and listed in Table 1 as follows: (1) carbon black (Vulcan XC-72R, Cabot); (2) High Surface Area Graphite ($HSAG_{300}$, Timcal); (3) Ordered Mesoporous Carbon (OMC, ACS Materials); (4) Graphite Nano Particles (GNP_{10}, ACS Materials); and (5) mesoporous Graphitized Nano Particles (GNP_{500}, Sigma Aldrich).

Pt/Carbon catalysts were prepared first by impregnating the carbon support with desired amount of hexachloroplatinic acid ($H_2PtCl_6.6H_2O$, Alfa Aesar) (99.99%) followed by a reductive process in 37 wt% formaldehyde stabilized with 10% methanol (Merck) at 80 °C for 1 h under reflux conditions. Reaction products were washed with ultrapure water (> 18.18 MΩ cm, ELGA Millipore), filtered through a 0.45 µm polycarbonate membrane (Sartorius) and finally dried in a vacuum oven (Thermo Scientific VT6025) at 80 °C and 50 mbar for 4 h. Nominal total metal loading on carbon supports were fixed to 40 wt.%. For comparison, commercial 40 wt.% Pt/C benchmark catalysts were purchased by QuinTech e.K. / Johnson Matthey (Pt/C_{JM}) and Heraeus GmbH ($Pt/C_{Heraeus}$).

Amount of the Pt loading on carbon support catalysts was estimated by thermo-gravimetric analysis (TGA) (NETZSCH STA 449 F3 Jupiter). Structural analysis of the catalysts was performed by X-ray diffractometer (XRD) (Bruker D8 Advance) equipped with Cu-K_{alpha} radiation (λ = 0.154 nm). Surface morphology and atomic/weight ratio of the catalysts were determined by scanning electron microscope (SEM) and energy dispersive X-ray spectroscopy (EDX) (Philips XL 40), respectively.

Electrochemical investigations were performed with a 0.205 cm^2 rotating glassy carbon disk and Pt ring electrode (RRDE) (Pine Research Instrumentation). Catalyst ink suspension was prepared as reported in a previous work [28]. Briefly, 2 mg of catalyst powder was dispersed in 1 ml of water:isopropanol mixture (1:2) and ultrasonicated for 5 min. About 20 µl of 1–10 wt% Nafion® (Ion Power, Inc.) containing ink was transferred onto the glassy carbon electrode. A total catalyst loading of about 80 ± 10 μg_{Pt} cm^{-2} was maintained for all systems.

Steady-state cyclic voltammograms (CV) were recorded with a bipotentiostat (Pine Research Instrumentation WaveDriver 20). A Pt wire and a saturated calomel electrode (SCE) were employed as counter and

reference electrode, respectively. The surface area of the counter Pt wire electrode was 4.7 cm^2. Electrochemical surface area (ECSA) of the catalyst was calculated by integrating hydrogen adsorption region in the CV between 0.005 and 0.36 V vs. NHE at 40 mV s^{-1} and by assuming that the charge induced by a monolayer of hydrogen atoms on Pt amounts 210 μC cm^{-2}. ORR measurements were performed in an oxygen-saturated 0.5 M H_2SO_4 electrolyte at 100–2500 rpm and a cathodic potential sweep of 5 mV s^{-1}. Accelerated degradation tests (ADT) were carried out in a N_2-saturated electrolyte and consisted of 10,000 cycles in the potential range of 0.4–1.4 V at 1 V s^{-1}. All potentials values were normalized to the normal hydrogen electrode (NHE) and iR corrected.

Typical GDE fabrication procedure was carried out as follows: 100 mg carbon-supported catalyst, 20 wt% PTFE and 10 wt% Nafion were suspended in a 1:2 water:isopropanol solvent mixture and stirred for 30 min. Addition of PTFE to Nafion was carried out to increase hydrophobic domains within reaction layer [29]. The catalyst ink was sprayed onto a carbon paper (Toray TGP-H-60) by air brush technique. Finally, as-coated GDE were sintered in an oven at 80 °C for 2 h. Freshly prepared working electrodes (0.5 cm^2 geometric area) were inserted in the GDE cell. All experiments were performed with a potentiostat (Zahner IM6eX) in deaerated and oxygen-saturated 0.5 M H_2SO_4 at 25 °C. A Pt wire and a RHE were employed as counter and reference electrode, respectively.

Transmission electron microscope (TEM) images of commercial carbon support and as-prepared Pt/C catalysts were taken at an acceleration voltage of 120 kV (Philips EM420). IL-TEM procedure was carried out by first dropping 10 μl of the catalyst ink onto a gold finder square grid (400 mesh, Plano). Then, the TEM grid was dried at 30 °C in vacuum oven for 2 h. About 10–15 reference points were identified on the grid in order to be able to recognize the same area during repeated TEM investigations. For electrochemical ADT procedure, the Pt/C-coated grid was immersed in 1 M H_2SO_4 and connected to potentiostat.

3. Results and discussion

3.1. Structural, thermal and surface morphology characteristics of Pt/C catalyst powder

All investigated 40 wt% Pt/C exhibited typical XRD pattern of face-centered-cubic (fcc) lattice structure as shown in Fig. 1 whereas first peak at 2θ = 23.5–26.45° especially in GNP and $HSAG_{300}$ samples is induced by (002) reflection of crystalline domains in carbon material. The clearly less pronounced diffraction peak observed at the other carbon systems is an indication for predominant amorphous constitution. Pt diffraction peaks at 2θ = 39.5°, 46.09°, 67.55° and 81.25° match well the standard Pt pattern (JCPDS, 04-0802).

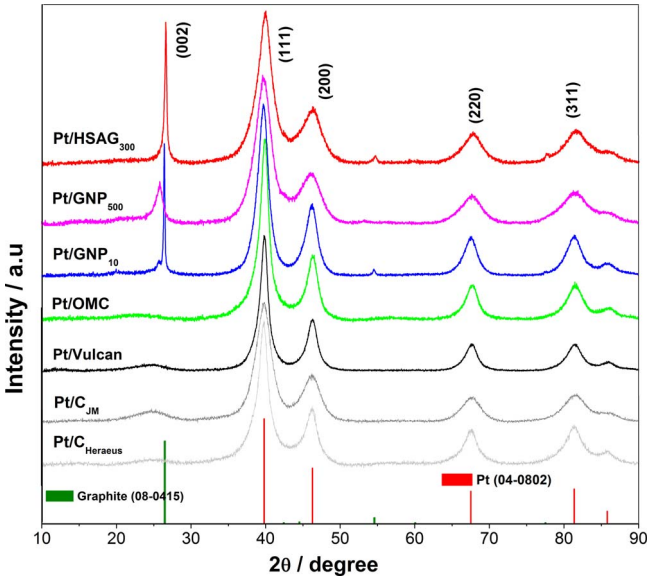

Fig. 1. XRD patterns of different carbon-supported Pt nanoparticles.

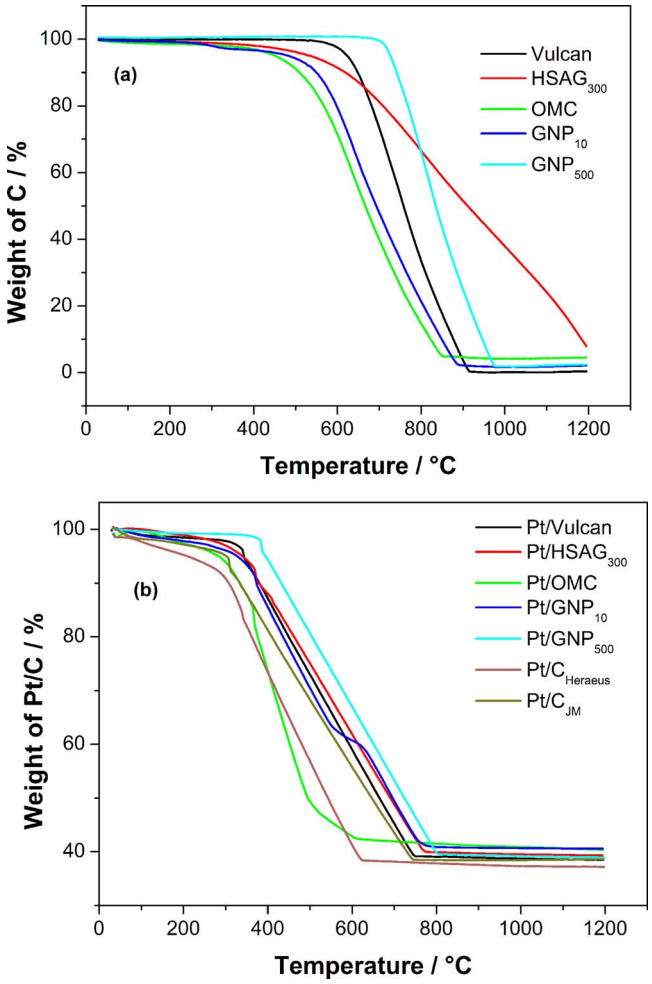

Fig. 2. TGA profile of normalized weight retention of different (a) carbons and (b) carbon-supported 40 wt% Pt catalyst.

TGA measurements at different carbons and carbon-supported Pt catalyst up to 1200 °C in air are presented in Fig. 2. During experiment on pure carbon materials, no substantial weight loss was observed at temperatures below 300 °C. Moreover, GNP_{500} exhibited outstanding thermal corrosion resistance (near to 100% mass retention) up to 700 °C for pure carbon and 400 °C for Pt/GNP system. Also Vulcan-based systems appear to be stable during thermal stress. For more accurate comparison, temperature values at which weight retention amounts 90% for carbon and 10% or 50% for Pt/C are listed in Table 2. One can recognize a clear correlation between corrosion affinity of carbon particle and their BET surface area; the higher the BET surface is, the faster the corrosion process takes place. Evaluation of mass loss rate in mg/°C was carried between well-defined values of T_{90} and T_{10}. A similar correlation between BET surface and TGA results is reported in the literature [30]. After Pt deposition, a significant shift of TGA curves towards lower temperature in the range of about 175–315 °C for $T_{90\%}$ can be observed for all Pt/C systems in Fig. 2b. The TGA results are summarized in Table 2. Especially Pt/OMC and Pt/C_{Heraus} are prone to thermal corrosion in air. Apparently, presence of densely well-dispersed Pt nanoparticle accelerates catalytic carbon oxidation to CO_2. Baturina et al. [31] studied influence of Pt concentration on Vulcan decomposition and concluded that onset temperature of weight loss decreased

Table 2
Summary of BET and TGA results.

Carbon	BET[b] $m^2 g^{-1}$	$T_{90\%}$ °C	$T_{10\%}$ °C	ΔT °C	Slope mg °C^{-1}	Catalyst Pt/Carbon	$T_{90\%}$ °C	$T_{50\%}$[a] °C	ΔT °C	Slope mg °C^{-1}	$\Delta T_{90\%}$ °C
Vulcan	240	640	877	237	−0.37	Pt/Vulcan	374	660	286	−0.27	266
$HSAG_{300}$	250	618	1182	564	−0.14	$Pt/HSAG_{300}$	378	693	315	−0.21	240
OMC	1000	505	820	315	−0.28	Pt/OMC	330	494	164	−0.25	175
GNP_{10}	690	550	850	300	−0.28	Pt/GNP_{10}	374	694	320	−0.11	176
GNP_{500}	100	742	946	204	−0.40	Pt/GNP_{500}	427	727	300	−0.13	315
						$Pt/C_{Heraeus}$	302	542	240	−0.17	–
						Pt/C_{JM}	326	646	320	−0.14	–

[a] For 40 wt% Pt/C systems, lower temperature limit of 50% weight was considered to keep an identical slope range as that of pure carbon.
[b] Data from carbon supplier.

with increasing Pt loading. Even in ambient air, large Pt concentration of 37.5 wt% can strongly attack π-conjugated polymer such as e.g. PEDOT and led to its super-oxidation [32]. The plateau at about 40% is an indication for both complete carbon combustion and effective amount of Pt loading on the different carbon substrates that was estimated to about 40 ± 0.8 wt%: Pt/Vulcan (39.1%), $Pt/HSAG_{300}$ (39.6%), Pt/OMC (40.8%), Pt/GNP_{10} (40.6%) and Pt/GNP_{500} (39.2%).

Fig. 3 shows TEM image of the different carbon before and after deposition with 40 wt% nanodisperse Pt as well as corresponding particle size distribution histograms. All investigated carbons obviously differ in morphology from each other. TEM images reveal a significant change of GNP_{10} structure and in less extend of GNP_{500} one after Pt deposition at 80 °C. As clearly seen in Fig. 3, Pt particles are uniformly dispersed on Vulcan, OMC and GNP_{500} substrates whereas catalyst agglomerates are visible on $HSAG_{300}$ and GNP_{10} materials. The average particle size of the different Pt/C systems is listed in Table 3. Based on comparative Gaussian curve fitting of the different histograms, following ranking with respect to quality of particle size distribution was established as follows: Pt/OMC > Pt/GNP_{500} > Pt/GNP_{10} > Pt/Vulcan > $Pt/HSAG_{300}$.

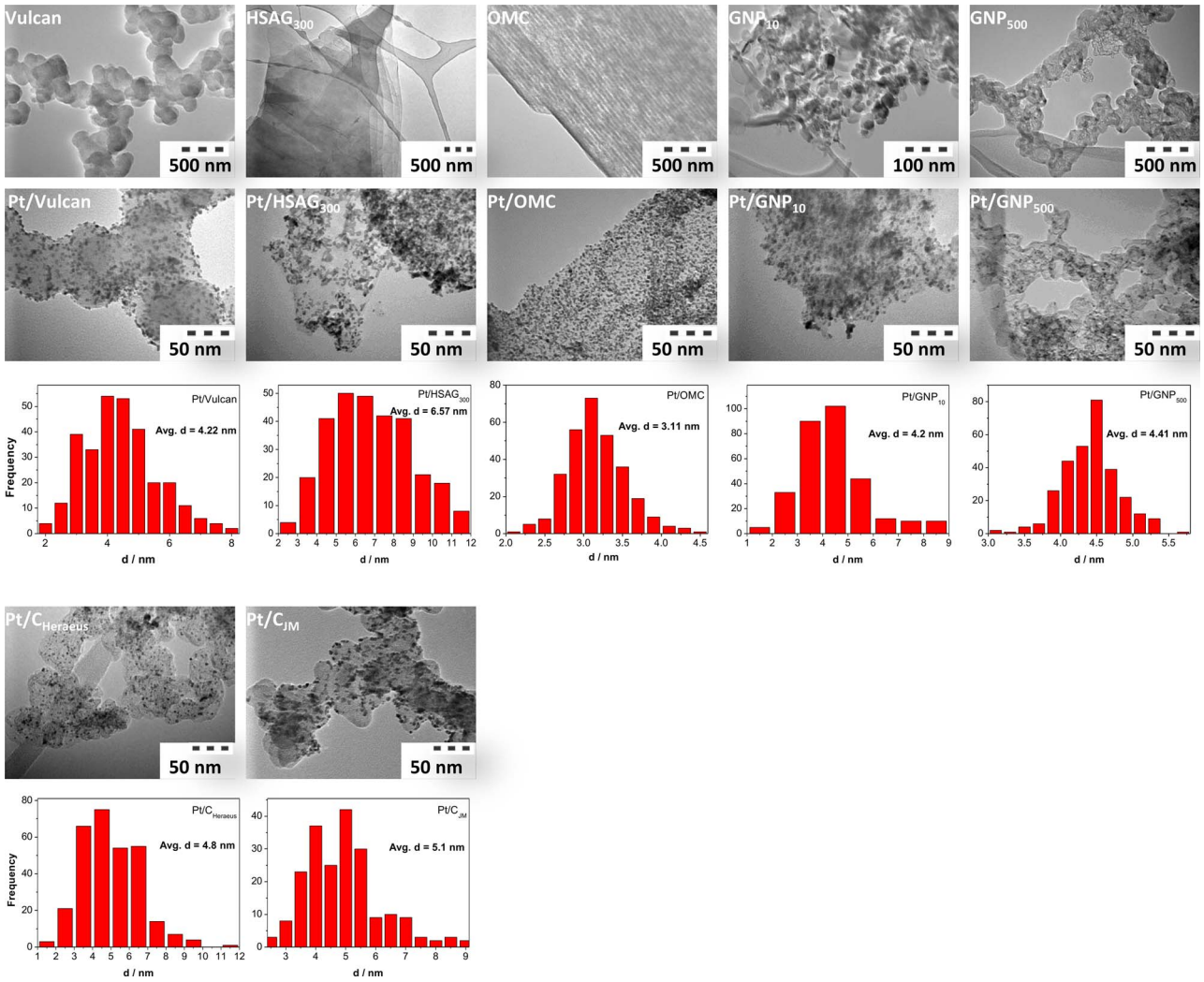

Fig. 3. TEM images of different carbons and 40 wt% Pt/C with corresponding Pt particle size distribution histograms based on evaluation of more than 300 particles for each sample.

Table 3
Summary of physical and electrochemical properties.

System	Pt $d_{avg.}$ nm	Tafel slope[a] mV dec^{-1}	N[b]	H_2O_2[c] %	Initial ECSA $m^2 g^{-1}$	SA[d] @ 0.8 V mA cm^{-2}	MA[d] @ 0.8 V mA g^{-1}	ECSA[e] ret. %
Pt/Vulcan	4.2	62-109	3.99	3.6	30.36	0.040	12.38	1.1
$Pt/HSAG_{300}$	6.5	60-103	3.89	2.6	26.69	0.151	40.51	0.2
Pt/OMC	3.1	60-120	3.86	1.9	32.29	0.108	34.89	29
Pt/GNP_{10}	4.2	57-125	3.99	1.0	21.43	0.315	67.65	4.8
Pt/GNP_{500}	4.4	60-120	3.98	1.6	26.69	0.300	80.13	2.6
$Pt/C_{Heraeus}$	4.8	70-122	3.88	3.1	12.93	0.245	31.67	0
Pt/C_{JM}	5.1	64-129	3.87	2.2	18.17	0.226	41.16	0.3

[a] First Tafel slope value for $0.1 < j(j_d\text{-}1)^{-1} < 5$ and second Tafel slope value for $10 < j(j_d\text{-}1)^{-1} < 100$.
[b] Number of electrons exchanged during ORR with linear regression R^2 of 0.994 (± 0.005).
[c] Estimated percentage of H_2O_2 production during ORR at 0.3 V, 1600 rpm.
[d] Specific (SA) and mass (MA) activity for ORR with an error of ± 0.002 mA cm^{-2} (SA) and ± 0.5 mA g^{-1} (MA).
[e] ECSA retention in percent after 10,000 cycles stability test.

3.2. Electrochemical characterization of Pt/C powder materials under RRDE conditions

3.2.1. Determination of optimal Nafion binder concentration

It is meanwhile accepted that evaluation and interpretation of ORR experiments are crucial issues that may take in account among other things electrolyte nature, catalyst particle size and more especially binder material concentration. Therefore Pt/OMC was used as reference system for demonstration and optimization of Nafion concentration within the reaction layer (see Fig. SI-1). Best compromise in terms of adhesion quality, binder content and electrochemical behavior was obtained with 1 wt% Nafion.

Fig. 4 shows cyclic voltammograms of the five as-prepared and two commercial carbon-supported 40 wt% Pt catalysts. In all CVs, typical electrochemical potential sweep responses for Pt such as $H_{ads/des}$, double-layer capacitance and oxide formation regions are well pronounced. Electrochemically active surface area (ECSA) of all catalysts was evaluated by integrating hydrogen desorption peak (see Table 3). Pt/OMC catalyst exhibited the highest ECSA (34.3 $m^2 g_{Pt}^{-1}$) and widest double-layer capacitance region that result from smallest Pt particles (3.11 nm) and largest specific BET surface area of the carbon support among investigated systems, respectively. Additionally, while similar onset potential values are observed for Pt-OH formation at Pt/Vulcan, $Pt/HSAG_{300}$, Pt/GNP_{10} and Pt/GNP_{500}, Pt/OMC oxidation started at lower potential. Subsequently, a positive shift of about 30 mV in the half-wave current region of Pt-OH reduction was observed at Pt/OMC compared to Pt/Vulcan and Pt/GNP_{500} which may positively influence the activity for ORR. Interestingly double-layer capacitance of all systems is quite identical, with exception of Pt/OMC, which is an indication for similar electrochemically active carbon surfaces. The difference in charge within hydrogen regions more especially in case of commercial samples reflects high discrepancy in catalyst accessibility even though the loading of investigated systems are quite similar. However, Pt particle sizes are not identical (see Table 3). We assumed that commercial catalysts were subjected to pre- or post-treatments that temporarily block Pt active sites e.g. by thin carbon layer [17].

Fig. 5a shows the linear sweep voltammograms (LSVs) response of the five as-prepared carbon-supported and two commercial Pt/C catalysts for ORR in oxygen-saturated sulfuric acid electrolyte. All catalysts exhibited well-defined kinetic-, mixed diffusion-kinetic- and diffusion-

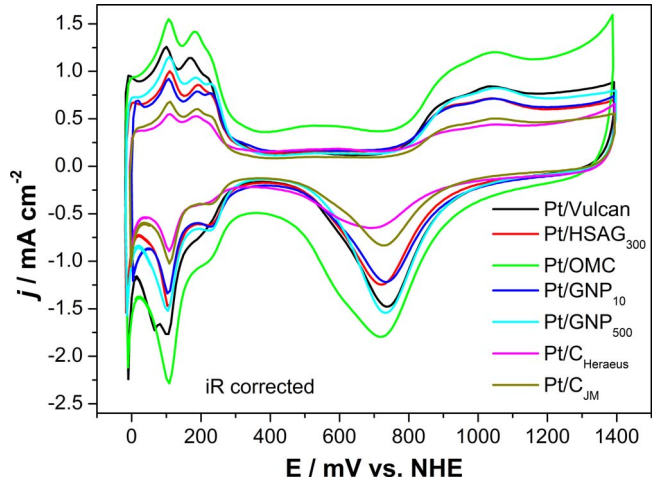

Fig. 4. CV of different 40 wt% Pt/C with 1% Nafion in N_2-saturated 0.5 M H_2SO_4 at 40 mV s^{-1} and 25 °C after 20 initial CVs.

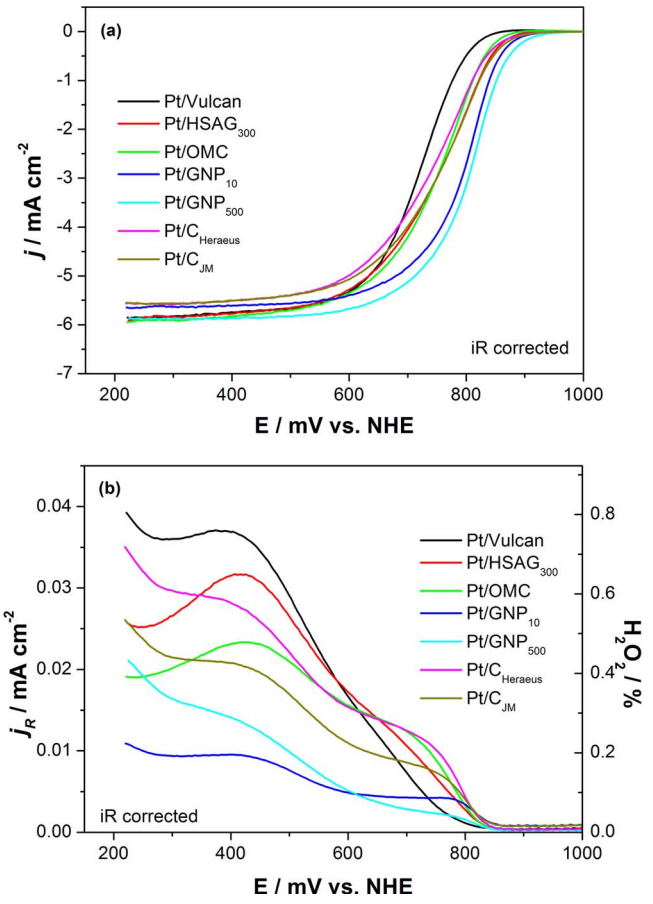

Fig. 5. Polarization curves of different 40 wt% Pt/C with 1% Nafion in O_2-saturated 0.5 M H_2SO_4 at 1600 rpm, 5 mV s^{-1} and room temperature at (a) GC disc and (b) Pt ring electrode at 1.2 V steady-state potential (collection efficiency = 0.23).

controlled regions. In the kinetic regime, ORR activity was evaluated at half-wave potential [33] where GNP-supported catalysts obviously show the best performance at 2.5 mA cm^{-2}. Based on the half-wave potential value, following ranking was obtained: Pt/GNP_{500} > Pt/GNP_{10} > > $Pt/HSAG_{300}$ = Pt/C_{JM} > Pt/OMC > $Pt/C_{Heraeus}$ > Pt/Vulcan. About 85 mV less overpotential for ORR was obtained at Pt/GNP_{500} compared to that at Pt/Vulcan (Table 3). Large difference in overpotential for ORR may be due to differences in surface activation, functional groups, pore size distribution, accessibility of active sites as well as affinity for $2e^-$ step with H_2O_2 formation. Amount of in situ H_2O_2 production was estimated by polarizing Pt ring electrode at 1.2 V according to [34] and is listed in Table 3. As expected, inverse trend is observed for H_2O_2 activity rate. The lower the H_2O_2 concentration, the higher the effective ORR rate is.

The mass and specific activity of the different carbon-supported catalysts were calculated by normalizing geometrical current density at 0.8 V towards Pt loading and ECSA values, respectively. As expected, GNP systems possess the highest specific and mass activities among investigated Pt/C systems. Since catalyst loading on GC electrode is identical for all systems, mass-normalized activity follows same trend as that observed by CV measurements. It should be pointed out that the values listed in Fig. 6 are strongly affected by the presence of 1% Nafion. In the case of Pt/OMC, a threefold higher value was calculated for the Nafion-free system compared to that for the 1% one.

Tafel slopes of ORR were obtained from polarization curves shown in Fig. 5a by plotting kinetic- and mixed kinetic transport controlled region current densities against potential (see Fig. 6b). For each sample, two different slopes can be identified whereas typical values of 60 and 120 mV dec^{-1} were obtained only for as-prepared Pt/OMC and Pt/GNP_{500} catalysts system (see Table 3). Tafel slopes at low current density for the as prepared catalysts system are 60 ± 2 mV dec^{-1},

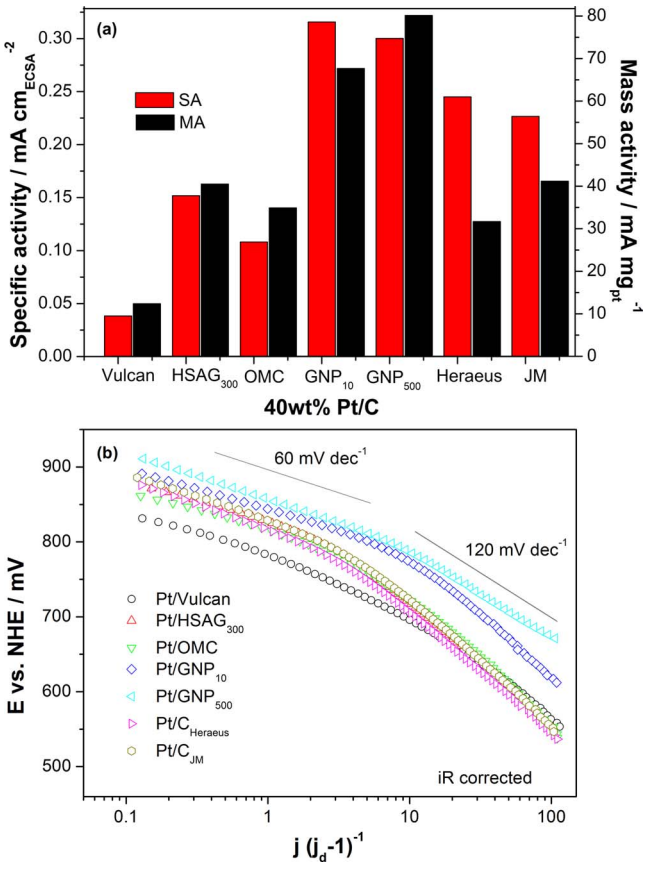

Fig. 6. Evaluation of different Pt/C catalysts activity for ORR in 0.5 M H_2SO_4: (a) specific and mass activity at 0.8 V and (b) Tafel slope from LSV measurement.

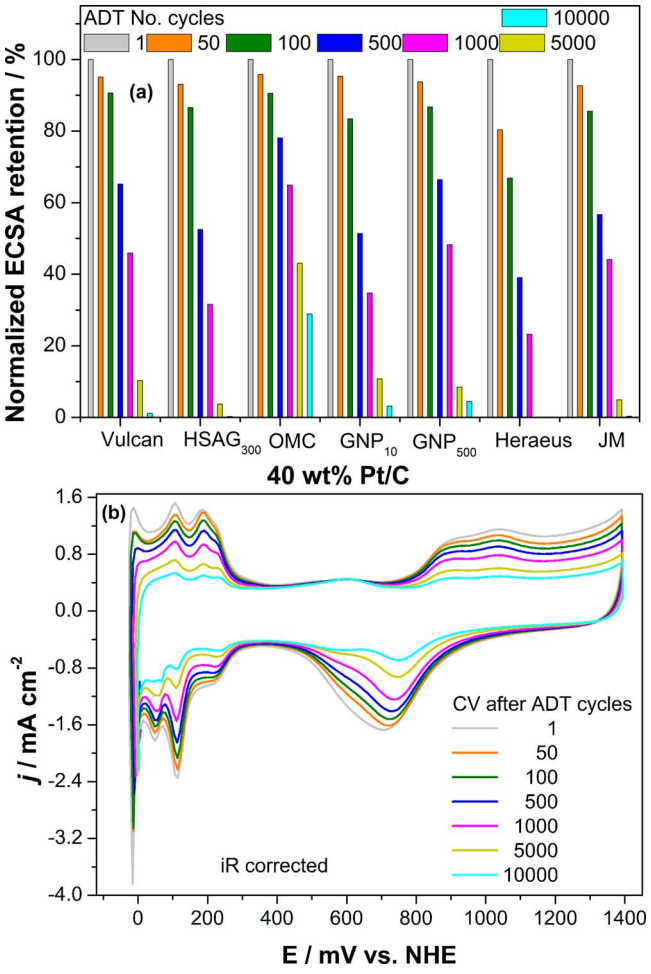

Fig. 7. (a) Influence of ADT cycle number on ECSA retention of different 80 μg cm^{-2} Pt/C catalysts + 10% Nafion. (b) Control CV of 40 wt% Pt/OMC with 10% Nafion during ADT in N_2-saturated 0.5 M H_2SO_4 at dE/dt = 40 mV s^{-1} and room temperature.

which are very close to − 2.3 RT/F [35]. The transition region from low to high slope value that is situated at about 800–750 mV results from enrichment/depletion of Pt surface hydroxide and oxide species (see CV in Fig. 4). Therefore, from a pure kinetics point of view, cell potential should preferably be set to higher values than 700 mV. At high current density values, Tafel slopes are nearly similar and those did not show any dependence on the type, shape, size and structural parameters of carbon support in all measured catalysts. Thus, it can be concluded that the ORR pathway and rate-determining step are the same on different type of the carbon supported Pt catalysts investigated here.

Fig. 7a shows ECSA-normalized retention behavior of the different catalysts after ADT cycles. While ECSA loss of as-prepared Pt/C and commercial Pt/C_{JM} catalysts amounts already about 10–18% after only 100 cycles, dramatical loss of about 30% is observed at $Pt/C_{Heraeus}$. After 1000 cycles, ECSA retention decreased to 55% for Pt/Vulcan, 69% for $Pt/HSAG_{300}$, 34% for Pt/OMC, 64% for Pt/GNP_{10}, 52% for Pt/GNP_{500}, 77% for $Pt/C_{Heraeus}$ and 55% for Pt/C_{JM}. After 10,000 cycles, only Pt/OMC exhibits a mentionable ECSA retention value of 25%, whereas Pt/GNP_{10} and Pt/GNP_{500} values shrank down to 3 and 5%, respectively. From all investigated systems, Pt on carbon with mesoporous structure appear to be more stable against corrosion. Fig. 7b show CV behavior of most performing Pt/OMC system in terms of ECSA retention. Since current density in double-layer capacitance region is moderately affected by ADT procedure, ECSA loss should predominantly result rather from Pt degradation mechanisms such as migration, Oswald ripening, coalescence, dissolution, precipitation and detachment [36] than from oxidation of OMC support.

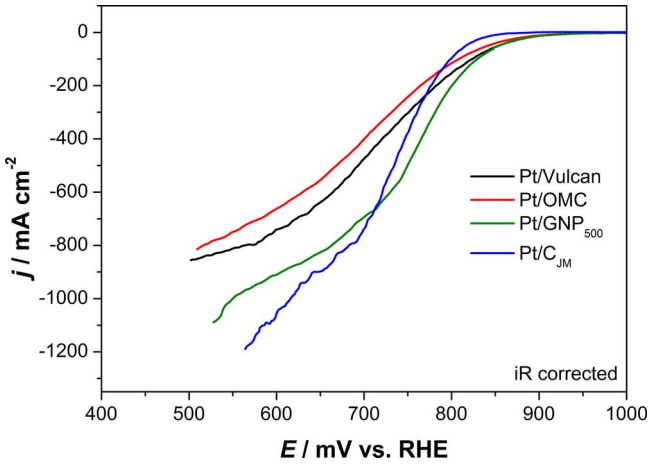

Fig. 8. LSVs of different 1 $mg_{Pt}cm^{-2}$ 40 wt% Pt/C GDEs with 10% Nafion in O_2-saturated 0.5 M H_2SO_4 at 5 mV s^{-1} and room temperature.

Vaarmets et al. [37] studies Pt-C(Mo_2C)850 °C stability at 50 mV s^{-1} in 0.5 M H_2SO_4. They recorded an ECSA loss of about 42% after 30,000 ADT cycles. However, direct comparison is not straight forwarded since mild conditions e.g. low scan rate was applied (50 mV s^{-1} vs. 1 V s^{-1} in this work). Stamatin et al. [38] examined Pt/SiC aging behavior in 0.1 M $HClO_4$ within two distinct potential windows at 0.5 V s^{-1}. Quite high degradation rate of about 20% after 9000 cycles was measured in relevant Pt oxide formation/reduction region between 0.6 and 1 V vs RHE. It should be noted that in both contributions, weight ratio of the binder material is not specified, which do not allow objective comparison.

3.3. Electrochemical characterization of Pt/C under GDE conditions

GDEs were fabricated with the two most stable as-prepared Pt/C systems namely Pt/OMC and Pt/GNP_{500} as well as Pt/Vulcan and Pt/C_{JM} as references and subjected to the same ADT procedure as in RRDE section. Fig. 8 shows polarization of Pt/C GDE for ORR and CVs of Pt/Vulcan GDE during ADT procedure in O_2-saturated 0.5 M H_2SO_4 electrolyte. As expected, ORR activity at GDE is at least two orders of magnitude higher compared to RRDE measurements due to higher oxygen concentration in the gas phase of the so-called three-phase boundary region (TPB) compared to that in liquid phase and is in agreement with Henry solubility (factor of 0.006). Although polarization curves exhibit evident discrepancies compared to RRDE plots shown in Fig. 5a, one can also here roughly distinguish mass transport-, mixed mass transport/kinetic- and kinetic-controlled regions for potential values lower than 700 mV, between 700 and 800 mV and between 800 and 850 mV, respectively. At 800 mV, Pt/GNP_{500} shows highest mass- and surface-normalized activity that confirmed results from RRDE experiments (see values in Table 4). Interestingly, in mass transport-controlled region, highest current density close to 1.2 A cm^{-2} was yielded at commercial Pt/C_{JM} compared to about 0.8 A cm^2 for the Pt/OMC-based GDE. This is a clear indication for more efficient transport of educts and products through reaction layer with spherical carbon particles compared to that with rather plane OMC ones (see TEM images in Fig. 3). Fig. 9a shows the trend of ECSA retention of GDEs at different ADT cycle number. Analogous to ADT results with RRDE, Pt/OMC system showed the best corrosion resistance with 67% ECSA retention followed by Pt/GNP_{500}, Pt/Vulcan and Pt/C_{JM}. In Fig. 9b, CVs of Pt/OMC are exemplary shown for demonstration.

Table 4
Summary of activity and stability results of Pt/C GDEs.

System	SA[a]@ 0.8 V mA cm^{-2}	MA[a] @ 0.8 V mA mg_{Pt}^{-1}	ECSA retention[b] %
Pt/Vulcan	43	154	51
Pt/OMC	64	118	67
Pt/GNP_{500}	96	205	61
Pt/C_{JM}	32	97	40

[a] Specific (SA) and mass (MA) activity for ORR with an error of ± 0.5 mA cm^{-2} (SA) and ± 2 mA g^{-1} (MA).

[b] ECSA retention after 5000 cycles stability test (0.4–1.4 V @ 1.0 V s^{-1}) relative to starting value.

3.4. Comparison of ADT results between RRDE and GDE test

A significant discrepancy in terms of ECSA retention was observed by comparing RRDE and GDE measurements as shown in Fig. 10. Although similar trend in which Pt/OMC clearly exhibits the highest stability followed by Pt/GNP_{500} and Pt/Vulcan, fluctuation between investigation at GDE and RRDE after 5000 ADT cycles is obvious. The enhancement in stability during GDE experiments is attributed to presence of 20% PTFE as additional binder compound in the GDE structure which apparently enhance Pt particle adherence on carbon support. As already mentioned in RRDE section, compromise between activity and stability has to be taking into consideration. Impact of binder structure and concentration on activity and stability was clearly demonstrated in this work. In order to get better insight into ECSA degradation mechanisms, identical location TEM (IL-TEM) investigation was conducted at most stable Pt/OMC and less stable Pt/Vulcan systems which possess

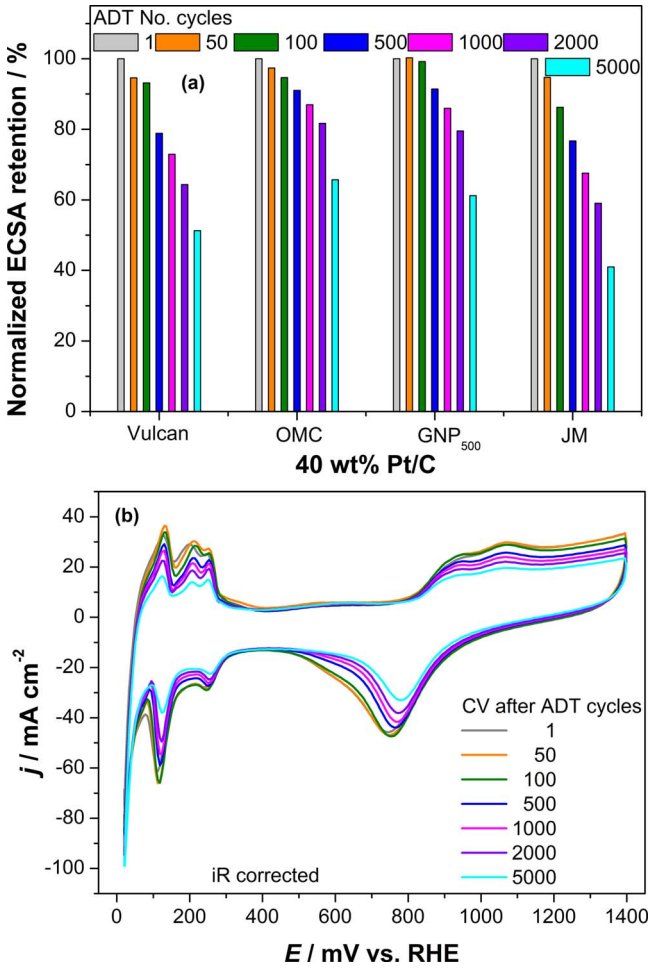

Fig. 9. (a) Influence of ADT cycle number on ECSA retention of different 1 mg cm^{-2} Pt/C GDEs with 10 wt% Nafion + 20 wt% PTFE. (b) Control CVs of 40 wt% Pt/Vulcan GDE in N_2-saturated 0.5 M H_2SO_4 at 40 mV s^{-1} and room temperature during ADT procedure.

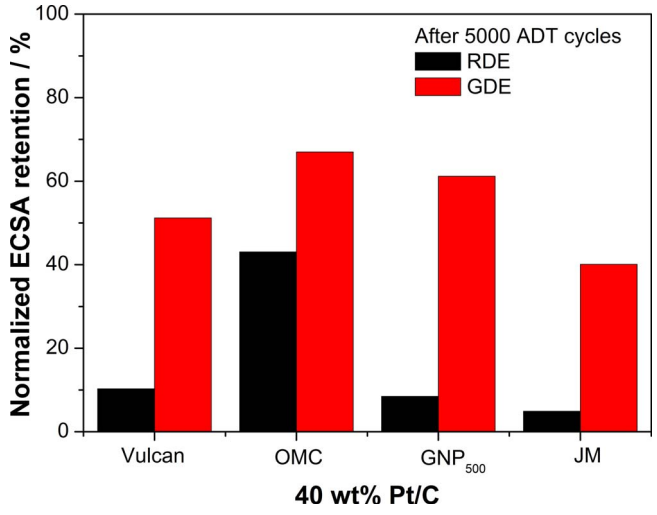

Fig. 10. Comparison of ECSA retention of 40 wt% Pt/C after 5000 ADT cycles (0.4–1.4 V @ 1 V s^{-1}) during RDE and GDE experiment in 1 M H_2SO_4.

very opposite morphology and therefore ideal for this time-consuming extensive investigation.

3.5. Post-mortem microscopic GDE inspection after ADT procedure

Fig. 11 shows SEM images and EDX mapping of selected GDE boundary region after ADT procedure where the grey area in the centre was in contact with electrolyte and the black one at the edge was covered by a sealing Parafilm layer and therefore not electrochemically active. The change from typically black color of as-prepared Pt/C catalyst layer still visible at electrode edge to bright grey reflects huge change in Pt concentration at the GDE/electrolyte interface that is more pronounced in case of Pt/C_{Vulcan}, Pt/C_{GNP500} and Pt/C_{JM} compared to more stable Pt/OMC GDE one as confirmed by EDX element mapping analysis. Increase in both particle size and concentration obviously led to radical optical change from black towards bright.

3.6. Interpretation of Pt/Vulcan & Pt/OMC degradation behavior by IL-TEM technique

For IL-TEM investigation, microporous Vulcan and mesoporous OMC carbon-supported Pt were the most appropriated candidate for time-consuming procedure. Selected IL-TEM images of these catalysts at different stage of ADT procedure are shown in Fig. 12. While no substantial change in average Pt particle size (5.2 nm) is visible on OMC substrate even after 10,000 cycles, dramatic evolution (4.7 to 30 nm) is obvious on Vulcan support. This is attributed to well-known mechanisms such as Pt migration, coalescence, dissolution, Ostwald ripening (growth of big particles of cost of smaller ones) and detachment. The latter mechanism occurs after reaching both critical size (25–35 nm) and consequently high contact angle value. Minor carbon corrosion is visible on TEM images, which well correlates with relatively stable current density observed in double-layer capacitance regions of both Pt/OMC and Pt/Vulcan CVs in Figs. 7b and Figure 9b, respectively. Particle size histogram presented in Fig. 12c is based on complete evaluation of Pt particles on Vulcan (about 150) and restricted to 300 representative ones for OMC support. For easier comparison, same scale was used for graphical evaluation of each selected steps. It should be noted that use of mesoporous carbon structure led to narrow Pt size distribution during chemical synthesis in formaldehyde in the range of 3–8 nm for Pt/OMC versus 1–10 nm for Pt/Vulcan. The maximal Pt particle size on OMC and Vulcan amounts 15 and 45 nm, respectively that was reached at 5000 and 10,000 cycles, respectively. While average catalyst size on Vulcan continuously increase with higher ADT cycle number from 4.7 up to 30 nm, average Pt size on OMC increase from 5.2 only to 6 nm after 5000 cycles and surprisingly decrease to 5.2 nm again after 10,000 cycles. This shift towards lower particle size can be explained by emergence of 48, 55 and 84 particles at 500, 5000 and 10,000 cycles within the range between 2 and 4 nm, respectively compared to only 13 for pristine material. Similarly, Hashé et al. [39] reported on Pt particle growth on mesoporous support until critical diameter of 5–7 nm during harsh start-up regime followed by shrinking process. A trial to follow Pt mass evolution on carbon supports within TEM image boundaries over ADT procedure by counting visible particles was not straightforward since $PA_{Pt,}10{,}000 > PA_{Pt,as\text{-}prepared}$ (see Table 5). This should be due to dissolution/migration of not visible Pt

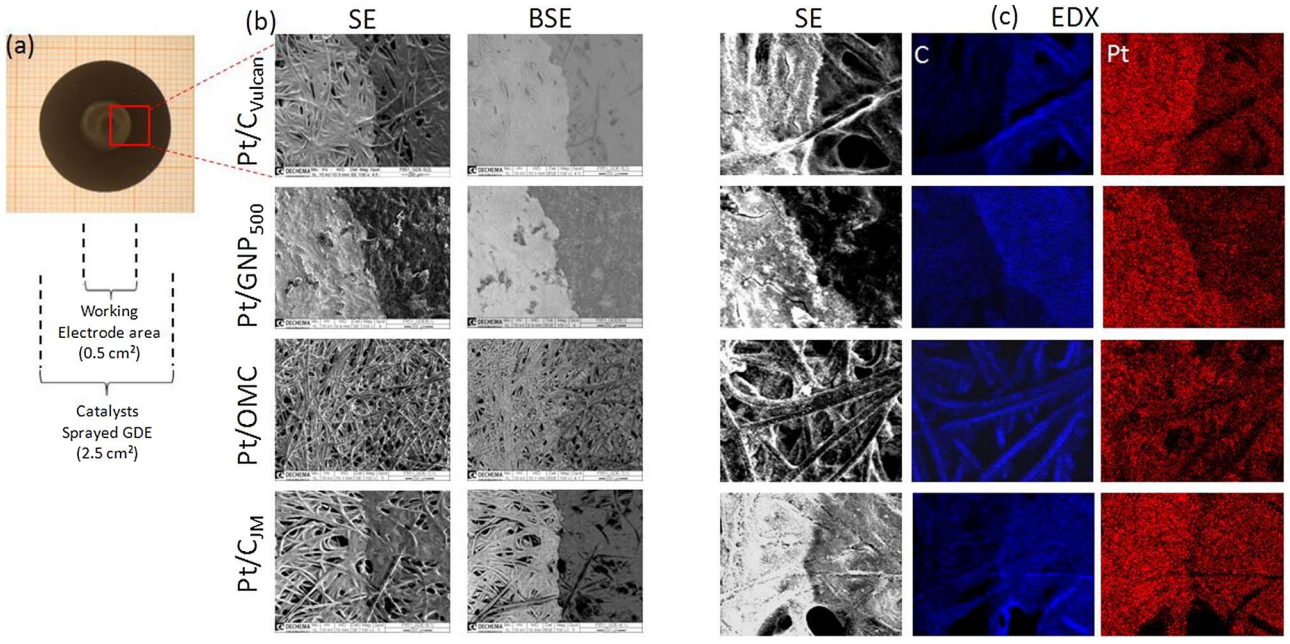

Fig. 11. (a) Optical microscopic GDE images with electrolyte-wetted grey area in the middle and non-electrochemically active electrode surface at the edge. (b) SEM images and (c) EDX mapping of selected transition region.

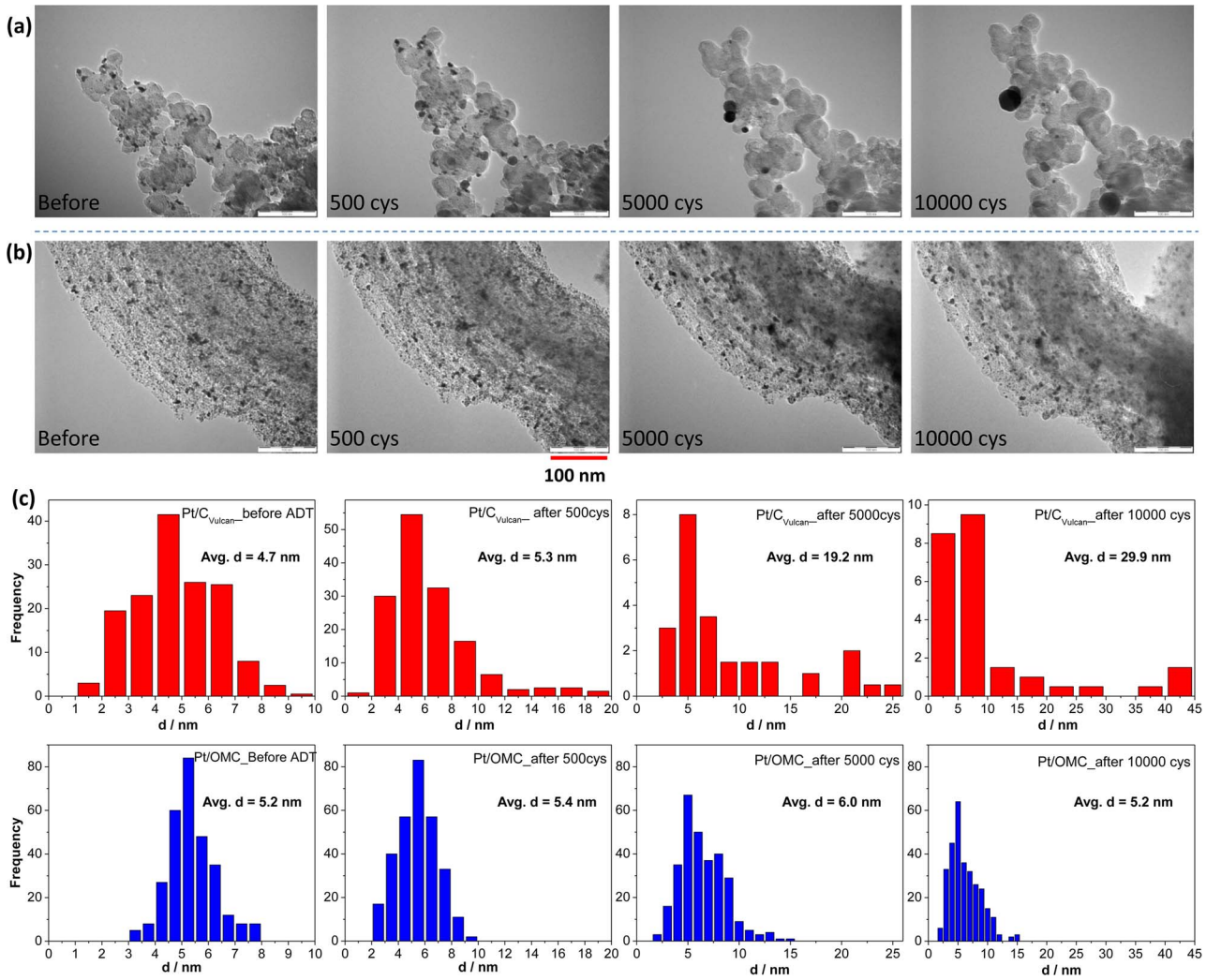

Fig. 12. IL TEM images of 20 wt% (a) Pt/Vulcan and (b) Pt/OMC before, and after (f.L.t.R.) 500, 5000 and 10,000 ADT cycles. (c) Corresponding Pt particle size distribution histograms.

Table 5
Calculation of projected area from IL-TEM images.

System	Projected area PA / nm^2			
	Initial	After 500 cycles	After 5000 cycles	After 10,000 cycles
Pt/Vulcan	5986	11788	4340	8313
Pt/OMC	7645	7988	9734	8588

particle situated on front electrode area but also to contribution of particle situated on the back side of Vulcan powder.

Interpretation of degradation mechanisms is highly complex since there are strongly depending on multitude of parameters such as synthesis route, initial particle size, degreeofalloying and temperature treatment of the catalyst, anchorage of functional groups, interaction with free radicals, morphology/constitution of the carbon support as well as nature/concentration of the binder/electrolyte and finally on profile of accelerated electrochemical degradation procedure. In this section, an attempt to correlate ADT results with IL-TEM images is presented. ECSA profiles during ADT procedure at 20 wt% Pt/Vulcan and Pt/OMC are shown in Fig. 13. Interestingly, ECSA behavior of Pt/Vulcan fits quite well calculated surface area/diameter mathematical function of ideal spherical particle that starts at 100 $m^2 g^{-1}$ for 1 nm particle (357 mg) and ends at 3% ECSA retention for 30 nm. Pt/OMC exhibits obviously higher ECSA retention, especially in 1000–10,000 ADT cycles region. During first 500 cycles, however, drastic ECSA loss of around 35 ± 2% can be observed at both Pt/Vulcan and Pt/OMC systems which is delimited by zone I. Since Pt particles on OMC carbon are very stable as confirmed by IL-TEM particle histogram shown in Fig. 12, drastic ECSA loss in early ADT procedure even at Pt/OMC should be accounted to dissolution of smaller Pt particles than 2 nm as suggested by calculated curve of spherical particle area included in Fig. 13. Further ECSA depletion of about 40% for Pt/Vulcan observed in 500–5000 transition region II is ascribed to Pt particle growth from about 5 to 10 nm. Further increase in particle size up to 30 nm during last 7000 cycles (region III) does not significantly affects ECSA value that lost 15 and 8% while relative residual ECSA amounts 2 and 30% at the end of the procedure in case of Pt/Vulcan and Pt/OMC, respectively. Positive effect of mesoporous structure of graphitic hollow spheres on stability of dispersed Pt was already impressively demonstrated by Meier et al. [36]. According to mathematical calculation, an overall increase in spherical particle diameter from 1 to 2 and from 2 to 5 nm would cause an impressive loss in ECSA of 50% and 30%, respectively with respect to initial value of 100 m^2.

4. Conclusions

In this work, different commercially available carbons have been tested regarding their both thermal and electrochemical activity/stability as support material for dispersed Pt nano-particle. XRD analysis confirmed presence of graphitic-rich domains in GNP and $HSAG_{300}$ samples while Vulcan, OMC and both commercial systems are predominantly

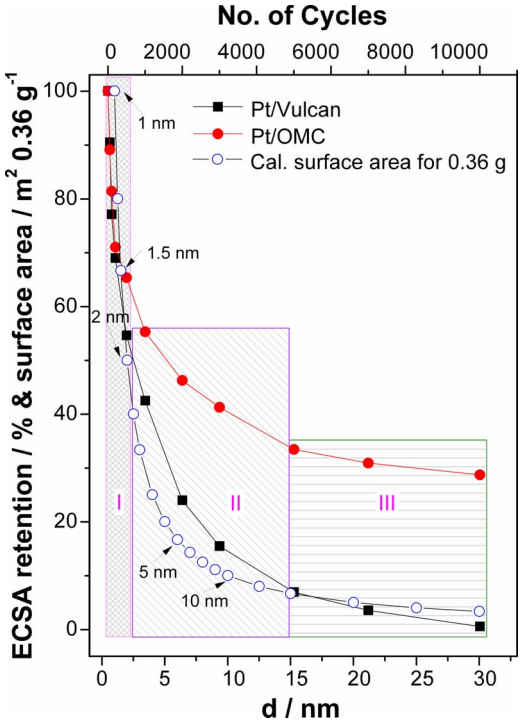

Fig. 13. ECSA behavior during ADT procedure (0.4–1.4 V @ 1 V s^{-1}) at 20 wt% Pt/Vulcan and Pt/OMC in 0.5 M H_2SO_4 on RRDE with 10 wt% Nafion as binder and calculated surface area of 357 mg spherical particles in function of their diameter as reference.

amorphous. TGA investigation revealed that activity of carbon corrosion is closely linked to amount of surface in contact with electrolyte. Carbon with large micropore domains and BET surface such as OMC and GNP_{10} were found to be more prone to corrosion. In that context, graphitization level seems to play a secondary role since more amorphous systems like Vulcan and GNP_{500} exhibited a higher thermal stability. RRDE and GDE half-cell measurements revealed highest activity of GNP-supported catalysts for ORR compared to other as-prepared and commercial samples. Unfortunately, they were more prone to Pt segregation at electrode/electrolyte interface and ECSA depletion as established during microscopic post-mortem analysis and electrochemical ADT procedure at GDE, respectively in comparison with Pt/OMC sample.

Actually, presence of ordered micropores on OMC carbon surface effectively hinders Pt migration/agglomeration/coalescence and as a consequence formation of larger particles which is beside Pt dissolution mainly responsible for ECSA depletion. According to IL-TEM images, it can be concluded that ECSA loss within first 500 cycles during severe pseudo start-stop ADT procedure between 0.4 and 1.4 V at 1 V s^{-1} is predominantly driven by Pt dissolution of smaller particle than 2 nm while at higher cycle numbers, particle growth plays a major role, especially on microporous carbon. On mesoporous carbon OMC structure, however, effect of particle growth with aging is quasi inexistent. Quantitative evaluation of Pt particle surface from IL-TEM histograms, however, does not correlate with ECSA behaviour. Pt detachment occurs presumably after crossing a critical particle diameter and contact angle value and in a less extend by carbon corrosion that play here a minor role in case of Vulcan and OMC supports. It can be concluded that high graphitization grade, spherical morphology, mesoporous surface structure (5–10 nm) as well as relative low BET surface ($\sim 100\ m^2\ g^{-1}$) were founded to be ideal properties for designing well-performing and highly stable Pt/C catalyst for low-temperature fuel cell applications. From practical and financial point of view, both mass transport properties as well as price of raw material should be considered as well, so that for test under DMFC stack conditions, relatively cheap spherical GNP_{500} was preferred to very expensive two-dimensional OMC structure. Relevant results will be published soon.

Acknowledgments

"Bundesministerium für Wirtschaft und Technologie (BMWi) via AiF" (17955 BG/3) is greatly acknowledged for financial support and project partners ZSW in Ulm and ICVT at Stuttgart University for excellent cooperation.

Appendix A. Supplementary data

Supplementary material related to this article can be found, in the online version, at doi:https://doi.org/10.1016/j.apcatb.2018.02.050.

References

[1] C. Lamy, C. Coutanceau, N. Alonso-Vante, Methanol-tolerant cathode catalysts for DMFC, in: H. Liu, J. Zhang (Eds.), Electrocatalysis of Direct Methanol Fuel Cells: From Fundamentals to Applications, Wiley, 2009, pp. 257–260.
[2] N. Bogolowski, J.F. Drillet, Appropriate balance between methanol yield and power density in portable direct methanol fuel cell, Chem. Eng. J. 270 (2015) 91–100.
[3] A.L. Dicks, The role of carbon in fuel cells, J. Power Sources 156 (2006) 128–141.
[4] P.T.Yu.W. Gu, J. Zhang, R. Makharia, F.T. Wagner, H.A. Gasteiger, Carbon-support requirements for highly durable fuel cell operation, in: F.N. Büchi, M. Inaba, T.J. Schmidt (Eds.), Polymer Electrolyte Fuel Cell Durability, Springer, 2009, pp. 29–53.
[5] D. Myers, M. Wilson, F. Garzon, D. Wood, P. Zelenay, K. More, K. Stroh, T. Zawodzinski, J. Boncella, J.E. McGrath, M. Inaba, K. Miyatake, M. Hori, K. Ota, Z. Ogumi, S. Miyata, A. Nishikata, Z. Siroma, Y. Uchimoto, K. Yasuda, K. Kimijima, N. Iwashita, Scientific aspects of polymer electrolyte fuel cell durability and degradation, Chem. Rev. 107 (2007) 3904–3951.
[6] P. Buffat, J.-P. Borel, Size effect on the melting temperature of gold particles, Phys. Rev. A 13 (1976) 2287–2298.
[7] W. Sheng, S. Chen, E. Vescovo, Y. Shao-Horn, Size influence on the oxygen reduction reaction activity and instability of supported Pt nanoparticles, J. Electrochem. Soc. 159 (2012) B96–B103.
[8] Y. Shao-Horn, W.C. Sheng, S. Chen, P.J. Ferreira, E.F. Holby, D. Morgan, Instability of supported platinum nanoparticles in low-temperature fuel cells, Top. Catal. 46 (2007) 285–305.
[9] N. Bogolowski, O. Ngaleu, M. Sakthivel, J.F. Drillet, Long-life bifunctional BaSrCoFeO3/C gas diffusion electrode, Carbon 119 (2017) 511–518.
[10] K. Kinoshita, Carbon, Electrochemical and Physicochemical Properties, John Wiley Sons, New York, 1988.
[11] S. Sharma, B.G. Pollet, Support materials for PEMFC and DMFC electrocatalysts—a review, J. Power Sources 208 (2012) 96–119.
[12] E. Antolini, Carbon supports for low-temperature fuel cell catalysts, Appl. Catal. B 88 (2009) 1–24.
[13] P. Trogadas, T.F. Fuller, P. Strasser, Carbon as catalyst and support for electrochemical energy conversion, Carbon 75 (2014) 5–42.
[14] J.B. Xu, T.S. Zhao, Mesoporous carbon with uniquely combined electrochemical and mass transport characteristics for polymer electrolyte membrane fuel cells, RSC Adv. 3 (2013) 16–24.
[15] H. Chang, S.H. Joo, C. Pak, Synthesis and characterization of mesoporous carbon for fuel cell applications, J. Mater. Chem. 17 (2007) 3078–3088.
[16] M.M. Bruno, F.A. Viva, M.A. Petruccelli, H.R. Corti, Platinum supported on mesoporous carbon as cathode catalyst for direct methanol fuel cells, J. Power Sources 278 (2015) 458–463.
[17] C. Galeano, J.C. Meier, V. Peinecke, H. Bongard, I. Katsounaros, A.A. Topalov, A. Lu, K.J.J. Mayrhofer, F. Schüth, Toward highly stable electrocatalysts via nanoparticle pore confinement, J. Am. Chem. Soc. 134 (2012) 20457–20465.
[18] A. Hayashi, H. Notsu, K. Kimijima, J. Miyamoto, I. Yagi, Preparation of Pt/mesoporous carbon (MC) electrode catalyst and its reactivity toward oxygen reduction, Electrochim. Acta 53 (2008) 6117–6125.
[19] S. Song, Y. Liang, Z. Li, Y. Wang, R. Fu, D. Wu, P. Tsiakaras, Effect of pore morphology of mesoporous carbons on the electrocatalytic activity of Pt nanoparticles for fuel cell reactions, Appl. Catal. B 98 (2010) 132–137.
[20] E. Lust, E. Härk, J. Nerut, K. Vaarmets, Pt and Pt–Ru catalysts for polymer electrolyte fuel cells deposited onto carbide derived carbon supports, Electrochim. Acta 101 (2013) 130–141.
[21] K. Vaarmets, J. Nerut, E. Härk, E. Lust, Electrochemical and physical characterisation of Pt-nanocluster activated molybdenum carbide derived carbon electrodes, Electrochim. Acta 104 (2013) 216–227.
[22] H.-J. Liu, J. Wang, C.-X. Wang, Y.-Y. Xia, Ordered hierarchical mesoporous-microporous carbon derived from mesoporous titanium-carbide-carbon composites and its electrochemical performance in supercapacitor, Adv. Energy Mater. 1 (2011) 1101–1111.
[23] N.I. Kim, J.Y. Cheon, J.H. Kim, J. Seong, J.Y. Park, S.H. Joo, K. Kwon, Impact of framework structure of ordered mesoporous carbons on the performance of supported Pt catalysts for oxygen reduction reaction, Carbon 72 (2014) 354–364.
[24] V. Grozovski, H. Kasuk, J. Nerut, E. Härk, R. Jäger, I. Tallo, E. Lust, Oxygen reduction at shape-controlled platinum nanoparticles and composite catalysts based on (100)Pt nanocubes on microporous–mesoporous carbon supports, Chem. Electro. Chem. 2 (2015) 847–851.

[25] T. Maiyalagan, A.B.A. Nassr, T.O. Alaje, M. Bron, K. Scott, Three-dimensional cubic ordered mesoporous carbon (CMK-8) as highly efficient stable Pd electro-catalyst support for formic acid oxidation, J. Power Sources 211 (2012) 147–153.
[26] C. Galeano, F. Schüth, J. Meier, K.J.J. Mayrhofer, J.F. Drillet, M. Sakthivel, T. Tesfu, V. Peinecke, Use of mesoporous graphite particles for electrochemical applications, US 2015 0017555 A1, (2015).
[27] G. Liu, X. Li, P. Ganesan, B.N. Popov, Development of non-precious metal oxygenreduction catalysts for PEM fuel cells based on N-doped ordered porous carbon, Appl. Catal. B 93 (2009) 156–165.
[28] M. Sakthivel, I. Radev, V. Peinecke, J.F. Drillet, Highly active and stable Pt3Cr/C alloy catalyst in H2-PEMFC, J. Electrochem. Soc. 162 (2015) F901–F906.
[29] M.L. Perry, T.F. Fuller, A historical perspective of fuel cell technology in the 20th century, J. Electrochem. Soc. 149 (2002) S59–S67.
[30] A.K. Kercher, D.C. Nagle, Monolithic activated carbon sheets from carbonized medium-density fiberboard, Carbon 41 (2003) 3–13.
[31] O.A. Baturina, S.R. Aubuchon, K.J. Wynne, Thermal stability in air of Pt/C catalysts and PEM fuel cell catalyst layers, Chem. Mater. 18 (2006) 1498–1504.
[32] J.F. Drillet, R. Dittmeyer, K. Jüttner, Activity and long-term stability of PEDOT as Pt catalyst support for the DMFC anode, J. Appl. Electrochem. 37 (2007) 1219–1226.
[33] C. Wang, L. Ma, L. Liao, S. Bai, R. Long, M. Zuo, Y. Xiong, A unique platinum-graphene hybrid structure for high activity and durability in oxygen reduction reaction, Sci. Rep. 3 (2013) 1–7.
[34] U.A. Paulus, T.J. Schmidt, H.A. Gasteiger, R.J. Behm, Oxygen reduction on a high-surface area Pt-Vulcan carbon catalyst-a thin-film rotating ring-disk electrode study, J. Electroanal. Chem. 495 (2001) 134–145.
[35] V.S. Murthi, R.C. Urian, S. Mukerjee, Oxygen reduction kinetics in low and medium temperature acid environment: correlation of water activation and surface properties in supported Pt and Pt alloy electrocatalysts, J. Phys. Chem. B 108 (2004) 11011–11023.
[36] J.C. Meier, C. Galeano, I. Katsounaros, J. Witte, H.J. Bongard, A.A. Topalov, C. Baldizzone, S. Mezzavilla, F. Schüth, K.J.J. Mayrhofer, Design criteria for stable Pt/C fuel cell catalysts, Beilstein J. Nanotechnol. 5 (2014) 44–67, http://dx.doi.org/10.3762/bjnano.5.5 https://www.beilstein-journals.org/bjnano/articles/5/5.
[37] K. Vaarmets, J. Nerut, S. Sepp, R. Kanarbik, E. Lust, Accelerated durability tests of molybdenum carbide derived carbon based Pt catalysts for PEMFC, J. Electrochem. Soc. 164 (2017) F338–F346.
[38] S.N. Stamatin, J. Speder, R. Dhiman, M. Arenz, E.M. Skou, Electrochemical stability and post-mortem studies of Pt/SiC catalysts for polymer electrolyte membrane fuel cells, ACS Appl. Mater. Interfaces 7 (2015) 6153–6161.
[39] F. Hasché, M. Oezaslan, P. Strasser, Activity, stability, and degradation mechanisms of dealloyed PtCu3 and PtCo3 nanoparticle fuel cell catalysts, Chem. Cat. Chem. 3 (2011) 1805–1813.